2. STRESS-STRAIN RELATIONSHIPS

2.1 Introduction

This chapter summarizes some typical mechanical properties of concrete under uniaxial, biaxial, and triaxial states of stress and also some general stress-strain characteristics of reinforcement steel. These data, which are essential for the generalized development of mathematical modelling of concrete and steel, serve two major purposes: (1) to give guidance on the proper type of material behaviour to be developed in mathematical modelling and (2) to provide data for the determination of the various material constants which appear in the models. However, it is crucial to know that most constitutive models are derived from data coming mainly from testing *average-age normal-strength concrete under short-term quasi-static loading*.

Concrete contains a large number of microcracks, especially at interfaces between coarser aggregates and mortar, even before any load has been applied. This property is decisive for the mechanical behaviour of concrete. The propagation of these microcracks during loading contributes to the nonlinear behaviour of concrete at low stress level and causes volume expansion near failure.

Many of these microcracks are caused by segregation, shrinkage, or thermal expansion in the mortar. Some microcracks may be developed during loading because of the differences in stiffness between aggregates and mortar. These differences can result in the strains in the interface zone several times larger than the average strain. Since the aggregate-mortar interface has a significantly lower tensile strength than mortar, it constitutes the weakest link in the composite system. This is the primary reason for the low tension strength of concrete material. From the preceding discussion one can expect that the size and texture of the aggregates will have a significant effect on the mathematical behaviour of concrete under various types of loading.

2.2 Uniaxial Behaviour of Concrete

2.2.1 Uniaxial compression test

Stress-strain curve. A typical stress-strain relationship for concrete subjected to uniaxial compression is shown in Figure (2.1a). The stress-strain curve has a nearly linear-elastic behaviour up to about 30 percent of its maximum compressive strength (f'_c). For stresses above this point, the curve shows a gradual increase in curvature up to about $0.75f'_c$ to $0.90f'_c$, whereupon it bends more sharply and approaches the peak point at f'_c. Beyond this peak, the stress-strain curve has a descending part until crushing failure occurs at some ultimate strain ε_u.

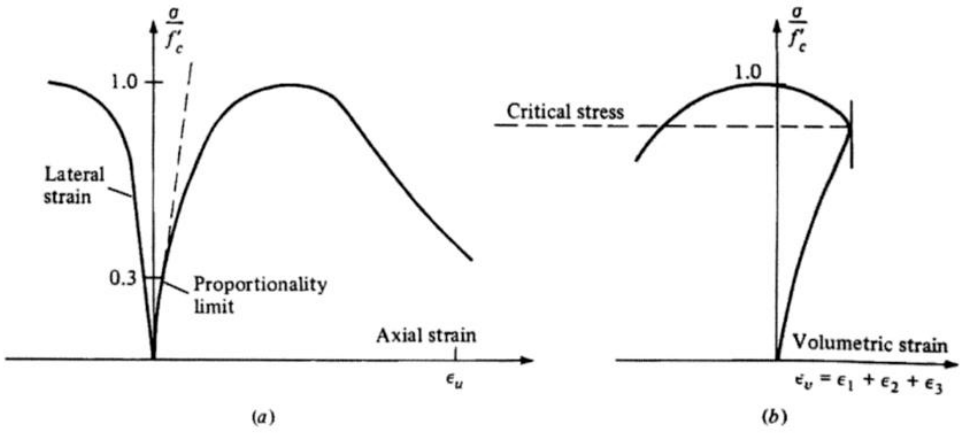

Figure 2.1 Typical plot of compressive stress vs. axial, lateral, and volumetric strain.

When the volumetric strain $\varepsilon_v = \varepsilon_1 + \varepsilon_2 + \varepsilon_3$ is plotted against stress, as shown in Figure (2.1b), initially the change in volume is almost linear up to about $0.75f'_c$ to $0.90f'_c$. At this point the direction of the volume change is reversed, resulting in a volumetric expansion near or at f'_c. The stress at which the volumetric strain ε_v is a minimum is termed *critical stress*.

The shapes of the stress-strain curves in Figure (2.1) are closely associated with the mechanism of internal progressive microcracking. For a stress in the region up to about 30% of f'_c, the cracks existing in the concrete before loading remain nearly unchanged. This indicates that the available internal energy is less than the energy required to create new microcrack surfaces. This stress level has been termed onset of localized cracking and has been proposed as a limit of elasticity.

For a stress between 30 to 50% of f'_c, the bond cracks start to extend due to stress concentrations at the crack tips. Mortar cracks remain negligible until a later stress range. For this stress range, the available internal energy is approximately balanced by the quick crack-release energy. At this stage, crack propagation is *stable* in the sense that crack lengths rapidly reach their final values if the applied stress is kept constant.

For a stress between 50 to 75% of f'_c, some cracks at nearby aggregate surfaces start to bridge in the form of mortar cracks. At the same time other bond cracks continue to grow slowly. If the load is kept constant, the cracks continue to propagate with a decreasing rate to their final lengths. For compressive stresses above about 75% of f'_c, the largest cracks reach their critical lengths. The available internal energy is now larger than the required crack-release energy. Thus, the rate of crack propagation will increase and the system is *unstable*, since complete disruption can occur even if the load is kept constant. The stress level of about 75% of f'_c is termed *onset of unstable fracture propagation* or *critical stress* since it corresponds to the minimal value of volumetric strain.

If we unload in the stress range between 50 and 75% of f'_c, the unloading curve exhibits some nonlinearity. If reloading takes place, a small characteristic hysteresis loop is formed, as shown in Figure (2.2). On the average, the unloading-reloading curve is fairly parallel to the initial tangent of the original curve. However, for unloading from stresses at about 75% of f'_c, the unloading-reloading curves exhibits strong nonlinearities (Figure 2.2), and a significant degradation of stiffness can also be observed. A reloading shows that the material-stiffness properties have changed drastically.

The progressive failure of concrete near f'_c is primarily caused by microcracks through the mortar. These microcracks join bond microcracks at the surfaces of nearby aggregates and form microcrack zones or internal damage. With increasing compressive strain, damage to concrete material continues to accumulate, and concrete enters the descending portion of its stress-strain curve, a region by the appearance of macroscopic cracks.

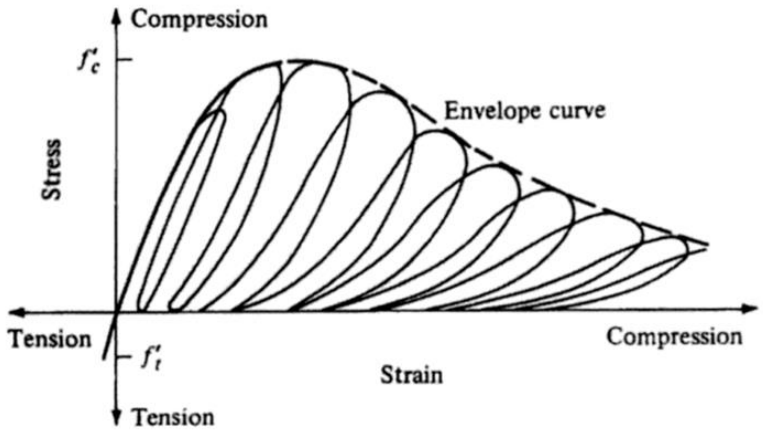

Figure 2.2 Response of concrete to uniaxial loading. *(Karsan and Jirsa, 1969.)*

The shape of the stress-strain curve is similar for concrete of low, normal, and high-strength, as shown in Figure (2.3). A high-strength concrete behaves in a linear fashion to a relatively higher stress level than the low-strength concrete, but all peak points are located close to the strain value of 0.002. On the descending portion of the of the stress-strain curve, higher-strength concretes tend to behave in a more *brittle* manner, the stress dropping off more sharply than it does for concrete with lower strength.

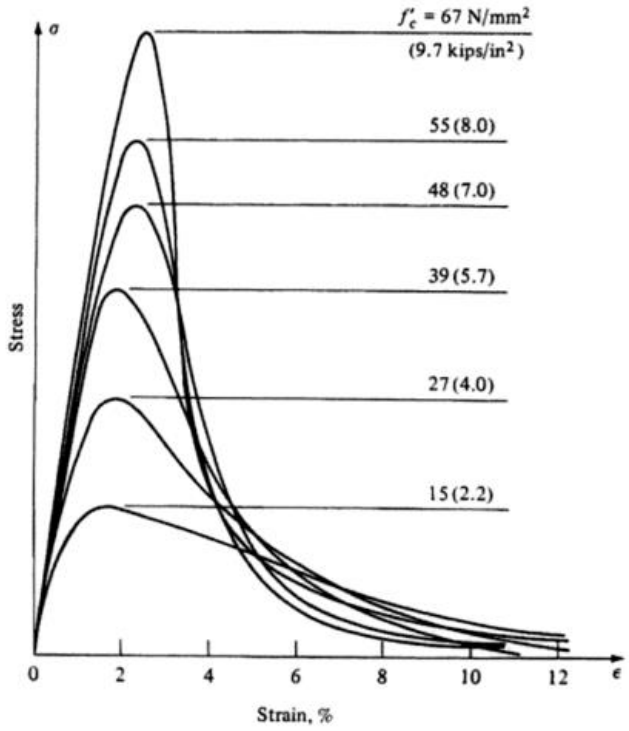

Fig. 2.3: Complete compressive stress-strain curve, (Wischers, 1978).

Modulus of elasticity. As shown in Figure (2.3), the initial modulus of elasticity of concrete is highly dependent on the compressive strength. In lieu of actual test data, the initial modulus of elasticity E_0 can be calculated with reasonable accuracy from empirical formulas. *This section will be treated extensively in the next chapter.* However, The ACI code adopted the following equation to calculate the concrete modulus of elasticity:

$$E_c \cong 4700\sqrt{f'_c} \qquad (2.1)$$

Poisson's ratio. Poisson's ratio v for concrete under uniaxial compressive loading ranges from about 0.15 to 0.22; a representative value is 0.19 or 0.20. Under uniaxial loading, the ratio v remains constant until approximately 80% of f'_c, at which stress the *apparent* Poisson's ratio begins to increase, see Figure (2.4). In the unstable crushing phase v even becomes larger than 0.5.

Cyclic behaviour. The behaviour of plain concrete subjected to cyclic compressive loading is shown in Figure (2.2). The degradation in both stiffness and strength for concrete with increasing number of applied cycles for a stress level of about $0.6f'_c$ is illustrated. For each cycle of unloading and reloading, a hysteresis loop is observed. The area of this loop decreases with each successive cycle but eventually increases before fatigue failure.

The stress-strain curve for monotonic loading serves as a reasonable envelope for the peak values of stress for concrete under cyclic loading.

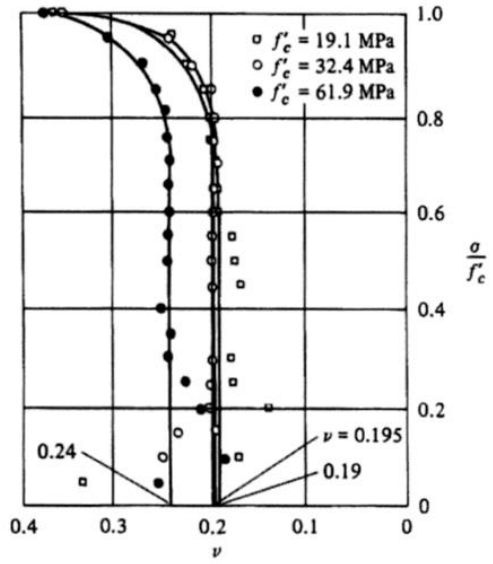

Fig. 2.4: Relation between stress-strength ratio and Poisson's ratio *v*.

Analytical model for cyclic loading. Typical hysteresis curves from experimental data (Figure 2.2) are idealized and approximated by straight-line segments for the hysteresis loop, see Figure (2.5). The size and shape of the loops are based on several of the experimental findings of Karsan and Jirsa (1969), summarized below.

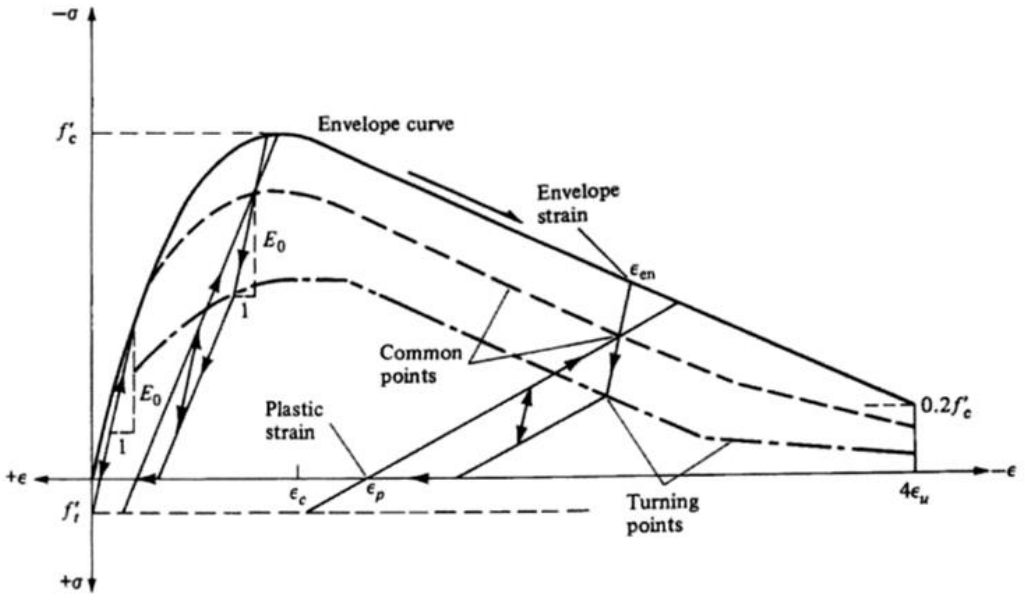

Fig. 2.5: A proposed model under cyclic behaviour, (Darwin and Pecknold, 1974).

The equation suggested by Saenz (1964)

$$\sigma = \frac{E_0 \varepsilon}{1+\left[\left(\frac{E_0}{E_S}\right)-2\right]\left(\frac{\varepsilon}{\varepsilon_C}\right)+\left(\frac{\varepsilon}{\varepsilon_C}\right)^2} \tag{2.2}$$

is used to describe the ascending branch of the stress-strain curves shown in Figure (2.5), and the falling branch is assumed to be a straight line passing through two points (f'_c, ε_c) and ($0.2f'_c$, $4\varepsilon_u$), where E_o is the tangent modulus of elasticity at zero stress, f'_c is the maximum compressive strength, ε_c is the corresponding strain at f'_c, ε_u is the crushing strain, and $E_s = f'_c/\varepsilon_c$.

An empirical relationship is assumed between the stain ε_{cn} on the envelope curve at unloading, termed the *envelope strain*, and the residual strain remaining at zero stress ε_p, termed the *plastic strain*. This relationship

$$\frac{\varepsilon_p}{\varepsilon_c} = 0.145\left(\frac{\varepsilon_{cn}}{\varepsilon_c}\right)^2 + 0.13\left(\frac{\varepsilon_{cn}}{\varepsilon_c}\right) \tag{2.3}$$

is incorporated into the model.

2.2.2 Uniaxial tension test

Figure (2.6) shows the stress-strain curves for concrete in uniaxial tension. All curves are nearly linear up to a relatively high stress level. The shape of the curves shows many similarities to the uniaxial-compression curves (Figure 2.3).

For stress less than 60% of the uniaxial tensile strength f'_t, the creation of new microcracks is negligible. Thus this stress level will correspond to the limit of elasticity; above this level, the bond microcracks start to grow. The value of *onset of unstable crack propagation* will be about 75% of f'_t.

The direction of crack propagation for uniaxial tension is transverse to the stress direction. The initiation and growth of every new crack will reduce the available load-carrying area, and this reduction causes an increase in the stresses at critical crack tips. The decreased frequency of crack arrests means that the failure in tension is caused by a few bridging cracks rather than by numerous cracks, as it is for compressive states of stress. As a consequence of the rapid crack propagation, it is difficult to follow the descending part of the stress-strain curve in an experimental test.

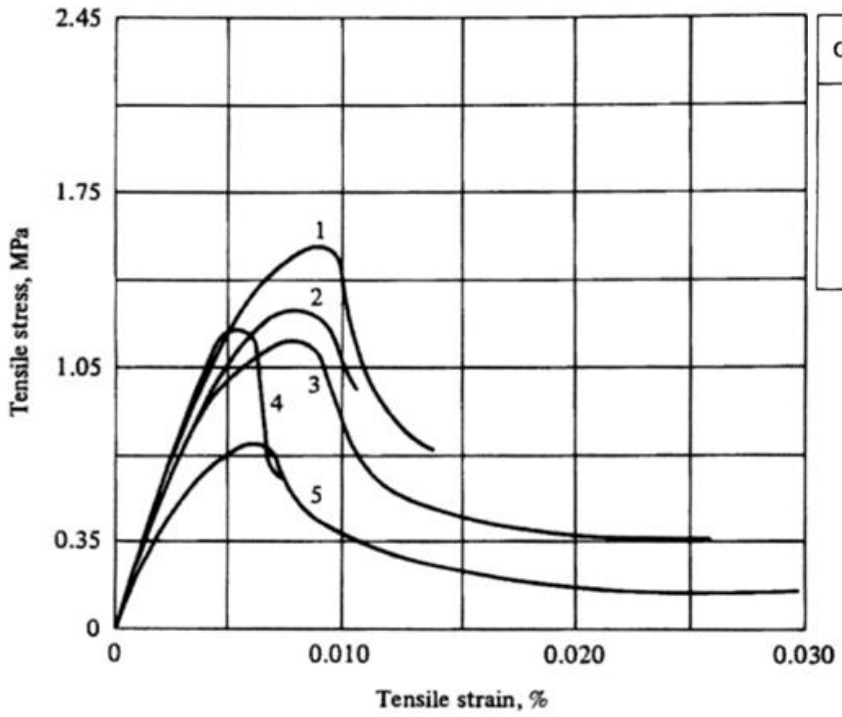

Curve	Aggregate		Age, in mo
	Type	Size, in	
1	Granite	$\frac{3}{8}-\frac{3}{16}$	2
2	Gravel	$\frac{3}{8}-\frac{3}{16}$	2
3	Gravel	$\frac{3}{16}$ – B.S.7	3
4	Gravel	$\frac{3}{8}-\frac{3}{16}$	2
5	Gravel	$\frac{3}{8}-\frac{3}{16}$	1

Figure 2.6 Resulting tensile stress-strain curves. ***(Hughes and Chapman, 1966.)***

The modulus of rupture f'_r or the split-cylinder strength (the Brazilian test) is often used to approximate the tensile strength of concrete. The value of the tensile strength varies widely but is normally taken as

$$Tensile\ Strength = k\sqrt{Compressive\ Stength} \qquad (2.4)$$

Where *k*, is a constant depenidng on the type of concrete, the type of test and the adopted standards.

According to ACI-318-1999 code, the modulus of rupture or flexural tensile strength is calculated by the following equation:

$f_r = 0.63\sqrt{f'_c}$ (ACI 318, 1999)

According to CSA-A23.3-94 code, the modulus of rupture is calculated by the following equation:

$f_r = 0.6\,\lambda\sqrt{f'_c}$ (CSA-A23.3-94)

The equation includes a factor (λ), which has different values according to the effect of concrete density on tensile strength

λ = 1.0 for normal density concrete.
λ = 0.85 for structural semi- low density concrete in which all the fine aggregate is natural sand.
λ = 0.75 for structural low-density concrete in which none of the fine aggregate is natural sand.

However, Nilson (1987) and Sarsam and Al-Azzawi (2010) proposed using k value approximately equals 0.9. The latter used a wide range of concrete strengths between 41 and 105 MPa.

For normal weight concrete the splitting tensile strength may be taken as follows:

$$f_{sp} = 0.68\sqrt{f'_c} \quad \text{(Nilson, 1987)}$$
$$f_{sp} = 0.58\sqrt{f'_c} \quad \text{(Wafa et al., 1992)}$$
$$f_{sp} = 0.70\sqrt{f_{ck}} \quad \text{(IS-456-2000)}$$
$$f_{sp} = 0.47\sqrt{f'_c} \quad \text{(Sarsam and Al-Azzawi, 2010)}$$
$$f_{sp} = 0.56\sqrt{f'_c} \quad \text{(ACI-318-11)} \qquad (2.5)$$

Where f'_c and f_{ck} are the characteristic cylinder and cube compressive strength in MPa, respectively.

The equation proposed by Sarsam and Al-Azzawi is more conservative and based on wider range of compressive strengths between 41 and 115 MPa.

2.3 Biaxial Behaviour of Concrete

2.3.1 Biaxial tests

Figures (2.7) to (2.9) show typical experimental stress-strain curves for concrete under biaxial compression (Figure 2.7), combined tension and compression (Figure 2.8), and biaxial tension (Figure 2.9).

First it is seen that the compressive strength increases for the biaxial-compression state. A maximum strength increase of approximately 25% is achieved at a stress ratio of $\sigma_2/\sigma_1 = 0.5$ and is reduced 16% at an equal biaxial-compression state ($\sigma_2/\sigma_1 = 1$). Under biaxial compression-tension, the compressive strength decreases almost linearly as the applied tensile stress is increased. Under biaxial tension, the strength is almost the same as that of uniaxial tensile strength, see Figure (2.10).

Second, concrete *ductility* under biaxial stresses has different values depending on whether the stress states are compressive or tensile as can be seen throughout Figures (2.7) to (2.9).

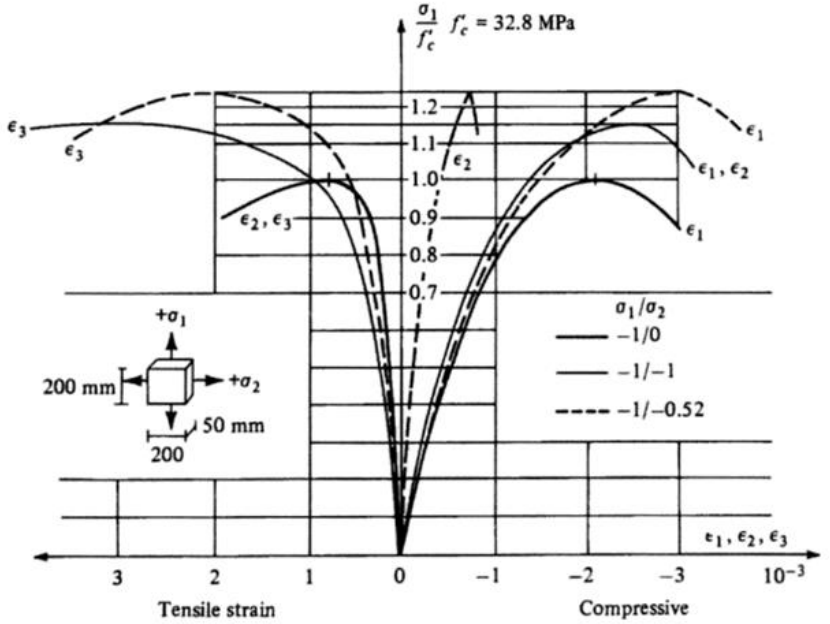

Figure 2.7 Stress-strain relationships of concrete under biaxial-compression test. *(Kupfer et al., 1969.)*

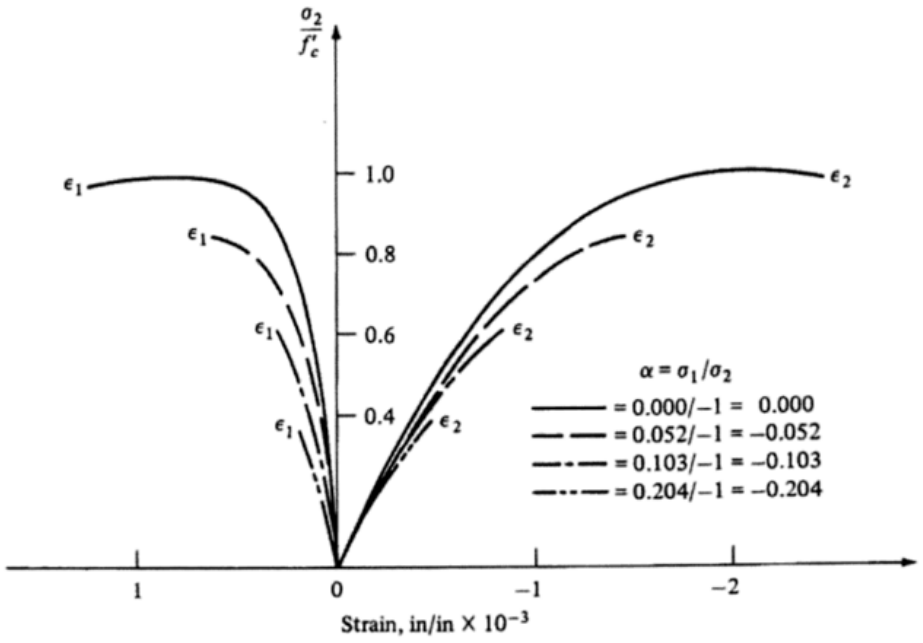

Figure 2.8 Experimental stress-strain curves for biaxial tension-compression. *(Kupfer et al., 1969.)*

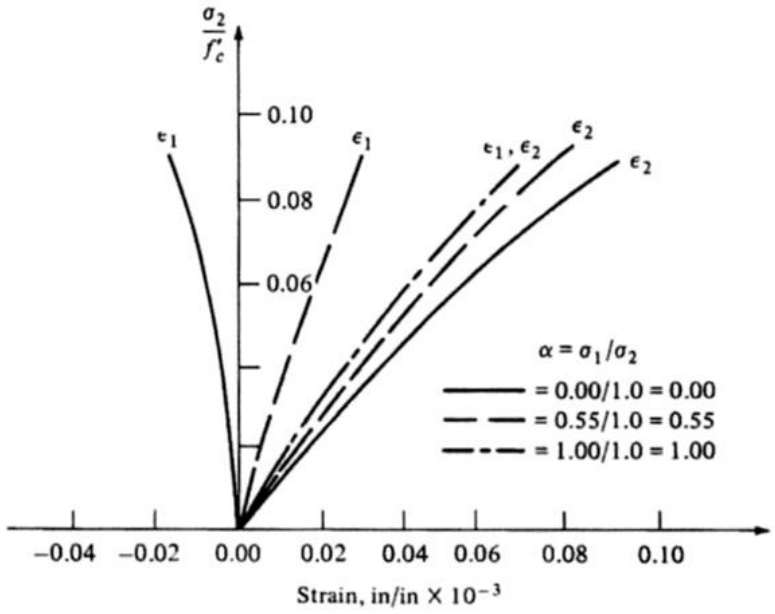

Figure 2.9 Experimental stress-strain curves for biaxial tension. *(Kupfer et al., 1969.)*

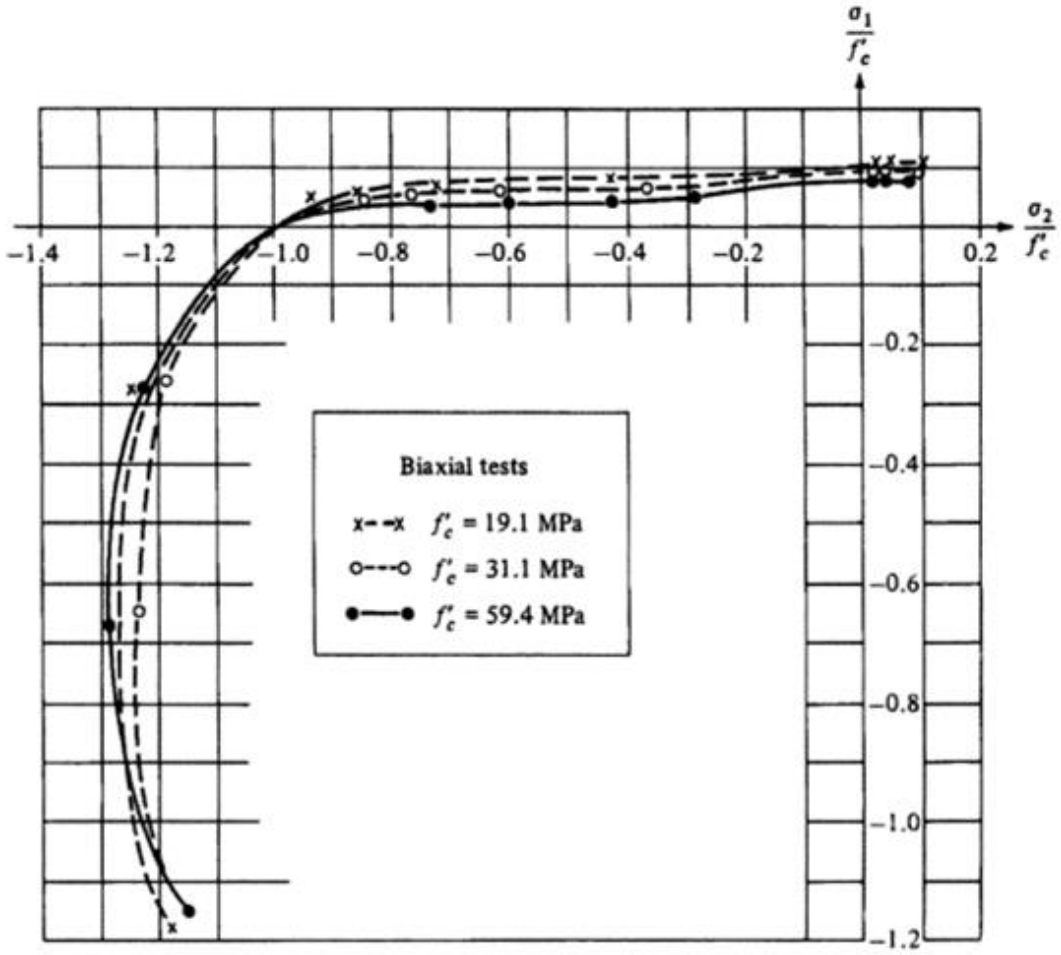

Figure 2.10 Biaxial strength envelope of concrete. *(Kupfer et al., 1969.)*

As the failure point is approached, an increase in volume occurs as the compressive stress continues to increase, as shown in Figure (2.11). This inelastic volume increase, called *dilatancy*, is usually attributed to progressive growth of major microcracks in concrete.

Failure of concrete occurs by tensile splitting with the fractured surface orthogonal to the direction of the maximum tensile stress or strain. Tensile strains are of crucial importance in the failure criterion and failure mechanism of concrete. Failures modes of biaxially loaded concrete are shown in Figure (2.12).

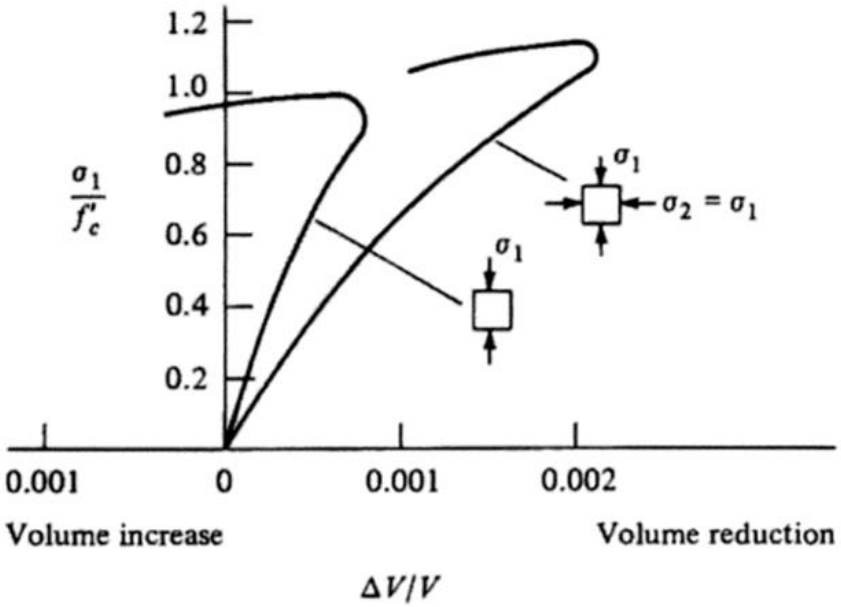

Fig. 2.11: Typical stress-strain curve for concrete volume change under biaxial compression.

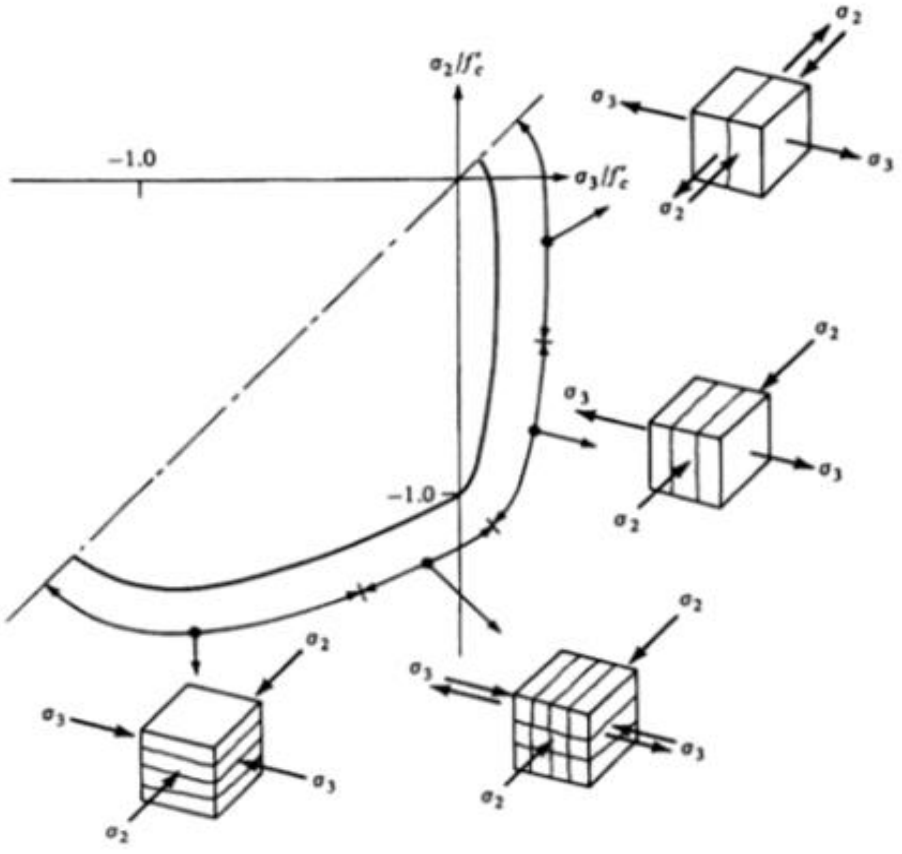

Figure 2.12 Failure modes of biaxially loaded concrete. *(Nelissen, 1972.)*

2.3.2 An equivalent uniaxial stress-strain relationship

The widely used function for simulation of stress-strain curves of concrete under biaxial states of stresses is based on a direct extension of Saenz's equation in compression in the form

$$\sigma = \frac{a\epsilon}{1+\left[\left(\frac{a\epsilon p}{\sigma p}\right)-2\right]\left(\frac{\epsilon}{\epsilon p}\right)+\left(\frac{\epsilon}{\epsilon p}\right)^2} \tag{2.6}$$

where

σ, ϵ = stress and strain in principal-stress direction,

σ_p, ϵ_p = experimentally determined values of maximum principal stress and corresponding strain,

a = experimentally determined coefficient representing initial tangent modulus and a linear relationship for tension.

This equation has a horizontal tangent modulus at the point of peak stress and corresponding strain (σ_p, ϵ_p). For uniaxial stress state, the point of peak stress and strain (f'_c , ϵ_c) as shown in Figure (2.5), and uniaxial initial elastic modulus is $a = E_0$.

For biaxial stress states, the maximum stress point (σ_p) is the value which can be determined from the biaxial strength envelope like that in Figure (2.10), and the corresponding value of maximum micro-compressive strain (ϵ_p) in the major direction can be fixed at about 3000 for uniaxial and biaxial compression states (Figure 2.7).

However, since under biaxial compression-tension the compressive strength (σ_p), decreases almost linearly as the tensile stress is increased, the corresponding decrease in compressive strain (ϵ_p) can be estimated by proportioning its value to the tensile-stress increase (Figure 2.8). Note that the value of (ϵ_p) in the minor direction will vary.

The biaxial compressive stress-strain curves of Figure (2.7) show increasing initial stiffness for increasing values of lateral compression, caused mainly by the effect of Poisson's ratio. Thus the strain measured in the same direction as the stress includes the contribution from the lateral direction. Similarly, Poisson's ration has a decreasing effect on the initial stiffness of the biaxial tensile stress-strain curves (Figure 2.9).

For a linearly elastic isotropic material, the biaxial stress-strain relation can be expressed as

$$\sigma = \frac{E_0\epsilon}{1-\nu\alpha} \tag{2.7}$$

where α = ratio of principal stress in orthogonal direction to principal stress in direction considered

E_0 = initial tangent modulus in uniaxial loading

ν = Poisson's ratio in uniaxial loading.

As an approximation, the *effective initial modulus $E_0/(1-v\alpha)$*, due solely to Poisson's effect, can be used as the initial modulus

$$a = \frac{E_0}{1-v\alpha} \tag{2.8}$$

in Equation (2.6), which describes the nonlinear biaxial stress-strain relationship of concrete. Since the biaxial stress-strain equation passes through the point of peak stress and strain (σ_p, ϵ_p) which accounts mainly for the microcrack confinement effect in the presence of biaxial stress, the tangent modulus, which is the slope at any point of the biaxial stress-strain curve ($E_t = d\sigma/d\epsilon$), includes both the microcrack confinement effect and Poisson's ratio effect.

Introducing the constant (2.8) into Equation (2.6) leads to

$$\sigma = \frac{E_0\epsilon}{(1-v\alpha)\left[1+\left(\frac{1}{1-v\alpha}\frac{E_0}{E_S}-2\right)\frac{\epsilon}{\epsilon_p}+\left(\frac{\epsilon}{\epsilon_p}\right)^2\right]} \tag{2.9}$$

where Es = σ_p / ϵ_p is the secant modulus of elasticity at peak stress, see Figure (2.13)

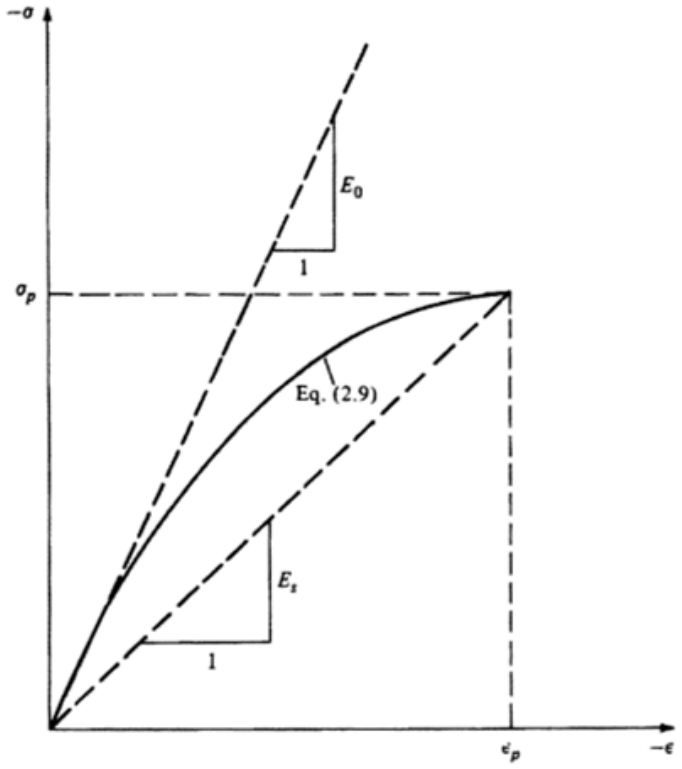

Figure 2.13 Equivalent uniaxial stress-strain curve.

The point of maximum compressive stress and strain (σ_p, ϵ_p) under biaxial loading is a function of the principal-stress ratio ($\alpha = \sigma_1/\sigma_2$), the uniaxial compressive strength (f'_c), and the strain at the peak uniaxial stress (ϵ_c). The values of the maximum stresses in the two principal directions σ_{1p} and σ_{2p} are obtained from the modified biaxial strength envelope of Kupfer and Gerstle (1973). It is assumed that the maximum tensile stress the concrete can withstand is the uniaxial tensile strength f'_t.

The biaxial strength envelope of Figure (2.10) is divided into four regions, which depends on the stress state as represented by the stress ratio α. Compressive stresses are assumed to be negative and tensile stresses positive, and the principal directions are chosen so that $\sigma_1 \geq \sigma_2$ algebraically.

The four regions of the strength envelope with the accompanying expressions for the maximum stresses σ_{1p}, σ_{2p} and their corresponding strains ϵ_{1p}, ϵ_{2p} are summarized as follows:

In the compression-compression region (σ_1 = compression, σ_2 = compression, $0 \leq \alpha \leq 1$)

$$\sigma_{2p} = \frac{1+3.65\alpha}{(1+\alpha)^2}\, \acute{f}_c \qquad \epsilon_{2p} = \epsilon_c \left(3\frac{\sigma_{2p}}{\acute{f}_c} - 2\right) \tag{2.10}$$

$$\sigma_{1p} = \alpha\sigma_{2p} \qquad \epsilon_{1p} = \epsilon_c \left[-1.6\left(\frac{\sigma_{1p}}{\acute{f}_c}\right)^3 + 2.25\left(\frac{\sigma_{1p}}{\acute{f}_c}\right)^2 + 0.35\frac{\sigma_{1p}}{\acute{f}_c}\right] \tag{2.11}$$

In the compression-tension region (σ_1 = tension, σ_2 = compression, $-0.17 \leq \alpha \leq 0$)

$$\sigma_{2p} = \frac{1+3.28\alpha}{(1+\alpha)^2}\, \acute{f}_c$$

$$\epsilon_{2p} = \epsilon_c \left[4.42 - 8.38\,\frac{\sigma_{2p}}{\acute{f}_c} + 7.54\left(\frac{\sigma_{2p}}{\acute{f}_c}\right)^2 - 2.58\left(\frac{\sigma_{2p}}{\acute{f}_c}\right)^3\right] \tag{2.12}$$

$$\sigma_{1p} = \alpha\sigma_{2p} \qquad \epsilon_{1p} = \frac{\sigma_{1p}}{E_0} \tag{2.13}$$

In the tension-compression region (σ_1 = tension, σ_2 = compression, $-\infty \leq \alpha \leq -0.17$)

$$\sigma_{2p} \leq 0.65\, \acute{f}_c$$

$$\epsilon_{2p} = \epsilon_c \left[4.42 - 8.38\,\frac{\sigma_{2p}}{\acute{f}_c} + 7.54\left(\frac{\sigma_{2p}}{\acute{f}_c}\right)^2 - 2.58\left(\frac{\sigma_{2p}}{\acute{f}_c}\right)^3\right] \tag{2.14}$$

$$\sigma_{1p} = \acute{f}_t \qquad \epsilon_{1p} = \frac{\sigma_{1p}}{E_0} \tag{2.15}$$

In the tension-tension region (σ_1 = tension, σ_2 = tension, $1 \leq \alpha \leq \infty$)

$$\sigma_{1p} = \acute{f}_t \geq \sigma_{2p} \qquad \epsilon_{1p} = \frac{\acute{f}_t}{E_0} \geq \epsilon_{2p} = \frac{\sigma_{2p}}{E_0} \tag{2.16}$$

The basic concept of this model is to treat the *biaxial stress-strain behaviour* of concrete as an ***equivalent uniaxial relation*** (Figure 2.13). According to this approach, the strain increment in each principal direction is evaluated solely by the principal-stress increment in the same direction; the corresponding tangent stiffness, which is a function of the principal-stress ratio α, accounts for all the biaxial effects. In this, Poisson's ratio is assumed to be a constant near 0.2. According to experimental evidence, this is fairly reasonable approximation up to about 80% of peak stress, but after this point it deviates progressively (See Figure 2.4).

The main advantages of this model are that it is simple and the required data are readily obtainable either from uniaxial tests on the concrete or from various biaxial tests reported in the literature. The model is mainly applicable to planar problems such as beams, panels, and thin shells, where the stress is predominantly biaxial. However, it is immediately apparent form Figure (2.11) that there is an abrupt volume increase near peak stress under biaxial compression. Such behaviour cannot be accounted for by the present equivalent uniaxial approach. Thus the model described will have little validity in three-dimensional situations.

2.3.3 Octahedral stress-strain relationships

The octahedral stresses and strains are defined by

$$\sigma_{oct} = \frac{1}{3}(\sigma_1 + \sigma_2 + \sigma_3)$$

$$\tau_{oct} = \frac{1}{3}[(\sigma_1 - \sigma_2)^2 + (\sigma_2 - \sigma_3)^2(\sigma_3 - \sigma_1)^2]^{1/2} \qquad (2.17)$$

$$\epsilon_{oct} = \frac{1}{3}(\epsilon_1 + \epsilon_2 + \epsilon_3)$$

$$\gamma_{oct} = \frac{2}{3}[(\epsilon_1 - \epsilon_2)^2 + (\epsilon_2 - \epsilon_3)^2(\epsilon_3 - \epsilon_1)^2]^{1/2} \qquad (2.18)$$

in which σ_{oct} and τ_{oct} are the octahedral (mean normal, or hydrostatic) and shear (or deviatoric) stresses, respectively, and ϵ_{oct} and γ_{oct} are the octahedral normal (or volumetric) and shear (or deviatoric) strains, respectively. This representation decouples the volume change and the distortional or shape-change portions of stress and strain; the stress increment $d\sigma_{oct}$ and strain increment $d\epsilon_{oct}$ associated with the volume change are related by the *tangent bulk modulus* K_t and the distortional quantities $d\tau_{oct}$ andn mmmn $d\gamma_{oct}$ by the *tangent shear modulus* G_t in the forms

$$K_t = \frac{d\sigma_{oct}}{3d\epsilon_{oct}} = \frac{E_t}{3(1-v_t)} \qquad G_t = \frac{d\tau_{oct}}{3d\gamma_{oct}} = \frac{E_t}{2(1+v_t)} \qquad (2.19)$$

The moduli K_t and G_t (or E_t, v_t) in Equations (2.19) are tangent values, which can be determined as the slopes of the volumetric (σ_{oct} - ϵ_{oct}) and deviatoric (τ_{oct} - γ_{oct}) stress-strain curves; according to this assumption, the bulk modulus is a function only of the volumetric and the shear modulus a function only of the deviatoric stress or strain levelnnnnnn

Deviatoric stress-strain relations. Figure (2.14) shows mean deviatoric (τ_{oct} - γ_{oct}) stress-strain curves obtained from biaxial-compression tests under four different stress ratios.

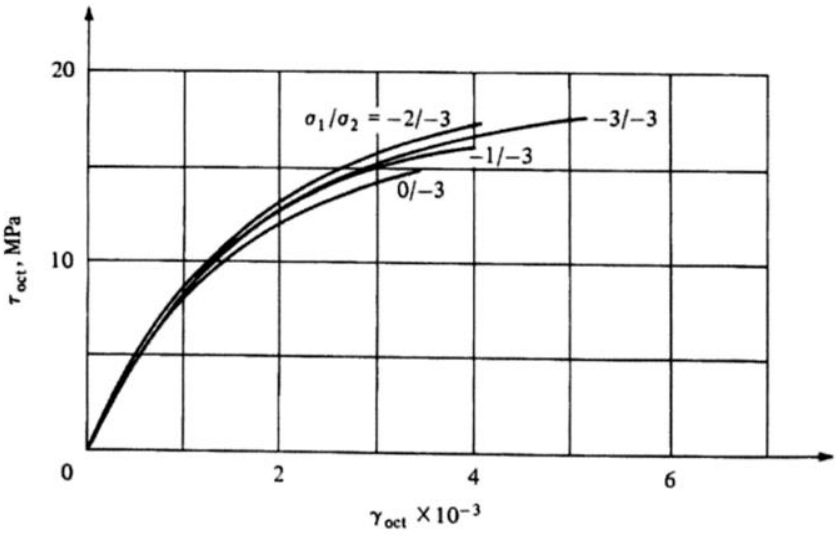

Figure 2.14 Octahedral shear-stress–strain relations from biaxial compression test.

To approximate these curves Gerstle (1981) proposed the exponential form

$$\tau_{oct} = \tau_{octp}\left[1 - exp\left(\frac{-G_0}{\tau_{octp}}\gamma_{oct}\right)\right] \tag{2.20}$$

in which τ_{octp} is the octahedral shear strength and G_0 is the initial shear modulus.

Differentiating (2.20), we obtain the tangent shear modulus

$$G_t = \frac{d\tau_{oct}}{d\gamma_{oct}} = G_0\, exp\left(\frac{-G_0}{\tau_{octp}}\gamma_{oct}\right) \tag{2.21}$$

Solving Equations (2.20) and (2.21) to eliminate γ_{oct} gives a relation between the tangent shear modulus and the stress level

$$G_t = G_0\left(1 - \frac{\tau_{oct}}{\tau_{octp}}\right) \tag{2.22}$$

Equation (2.22) shows that the assumption of an exponential τ_{oct} - γ_{oct} curve leads to a shear modulus which decreases linearly for its initial value G_0 for τ_{oct} = 0 to zero at failure, as shown by the solid line in Figure (2.15).

Equation (2.22) and the solid line of Figure (2.15) indicate no linear range of concrete behaviour, in fact, tests show that the shear stiffness decreases more slowly than indicated by Equation (2.22), as represented by the dashed curve of Figure (2.15).

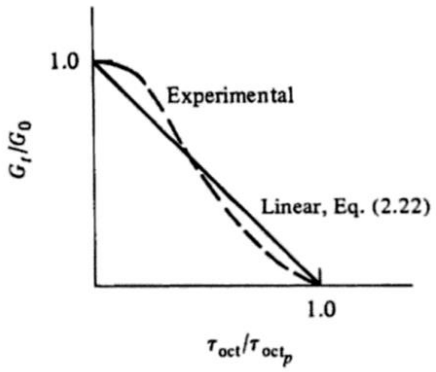

Figure 2.15 Variation of tangent shear modulus with octahedral shear stress. *(Gerstle, 1981.)*

The initial shear modulus G_0 in Equation (2.22) can be obtained through the second equation of (2.19) from a uniaxial-compression test, which allows determination of the modulus of elasticity E_0 and Poisson's ratio v_0. Alternatively, E_0 can be obtained from the ACI code equation (2.1), and v_0 for concrete is often assumed to be 0.2.

The deviator strength τ_{octp} can be obtained from a biaxial strength envelope, as shown in Figure (2.10). To find τ_{octp} form this figure, we reduce the second equation of (2.17) to the biaxial case by setting σ_3 =0 and letting the biaxial stress ratio $\alpha = \sigma_1/\sigma_2$

$$\tau_{octp} = \frac{\sqrt{3}}{2}\sqrt{1-\alpha+\alpha^2}\,\sigma_{2p} \tag{2.23}$$

in which σ_{2p} is the major principal stress at failure for the stress ratio α. For the strength variation shown in Figure (2.10) for different stress ratios, the deviator strength τ_{octp} can be calculated using Equation (2.23). Knowledge of the uniaxial compression strength f'_c and use of a suitable strength envelope, as shown in Figure (2.10), permit determination of the deviator strength τ_{octp} for any stress ratio.

Volumetric stress-stress rations. Quantitative evidence of the volumetric behaviour of concrete under biaxial compressive-stress states varies widely. It has been generally accepted that under increasing compression, the material first compacts and eventually dilates due to microcracking (Newman and Newman, 1969); but it is not at all clear at what stage this occurs (Gerstle, 1981). Figure (2.16a and b) shows results from two supposedly identical biaxial-test series on one concrete (Two different labs). In the first one, the dilatation occurs immediately before failure, i.e., when $\sigma_{oct} = \sigma_{octp}$; in the second one, this dilatation begins at stress levels from 70 o 85% of failure. It appears that the details of load application and measurement ay have great influence on the observed data.

The variation of moduli corresponding to these two series of stress-strain curves appears quite different, as shown by the dashed line in Figure (2.17). Possible linearizations are shown by solid and dash-dot lines in Figure (2.17a). Here again, trade-offs between reality and simplicity are indicated; because the volumetric portion is less significant in biaxial than in triaxial cases, and because of the apparent vagueness of experimental evidence, considerable simplification may be in order.

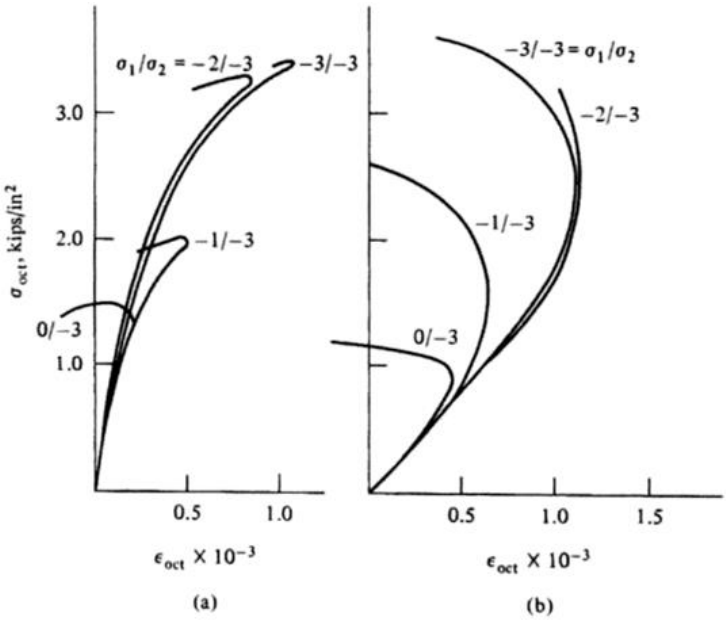

Figure 2.16 Volumetric stress-strain curves from biaxial tests: (*a*) Munich tests. *(Linse and Aschl, 1976.)* (*b*) Berlin tests. *(Schickert and Winkler, 1977.)*

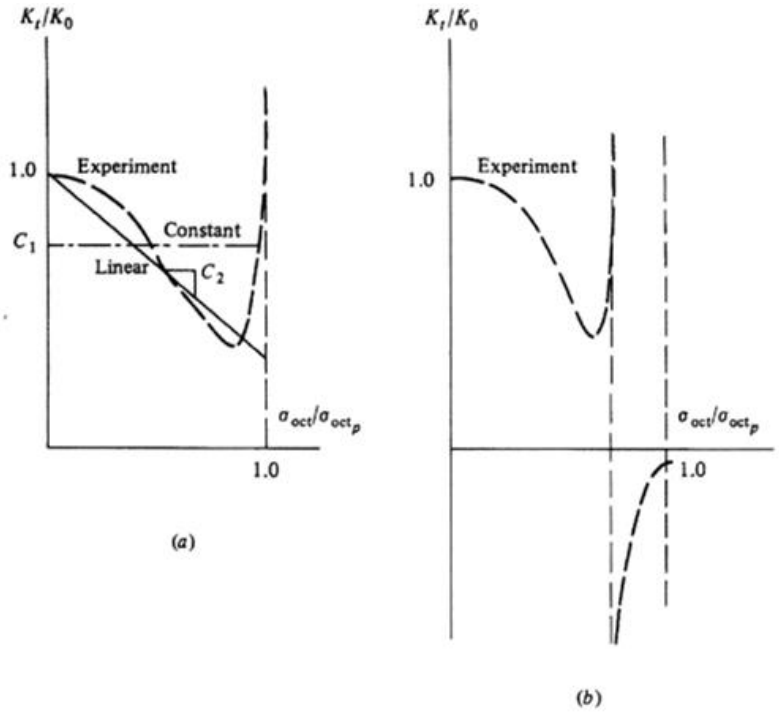

Figure 2.17 Variation of tangent bulk modulus with octahedral normal stress: (*a*) Munich tests; (*b*) Berlin tests. *(Gerstle, 1981.)*

The following possible approximations shown in Figure (2.17a) are proposed by Grestle (1981): constant mean bulk modulus, shown by dash-dot line in Figure (2.17a),

$$K_t = C_1 K_0 \tag{2.24}$$

and linearly varying bulk modulus, shown by solid line in Figure (2.17a),

$$K_t = K_0 \left(1 - C_2 \frac{\sigma_{oct}}{\sigma_{octp}}\right) \tag{2.25}$$

where K_0 = initial bulk modulus
C_1, C_2 = experimental constants
σ_{octp} = hydrostatic stress corresponding to failure

Using the first equation of (2.17), with $\sigma_3 = 0$ and $\alpha = \sigma_1/\sigma_2$, we have

$$\sigma_{octp} = \frac{1}{3}(1 + \alpha)\, \sigma_{2p} \tag{2.26}$$

The variation of bulk modulus shown in Figure (2.17b) leads to a much more complicated formulation, which may not be warranted in the view of the conflicting experimental evidence.

Secant shear modulus. Using results from many tests, Cedolin et al. (1977) formulated the variation of the secant shear modulus G_s as

$$\frac{G_s}{G_0} = 0.81(2^{-500\gamma_{oct}}) - 0.5\gamma_{oct} + 0.19 \tag{2.27}$$

This equation is independent of the concrete strength τ_{octp}; its variation is shown as the solid curve in Figure (2.18).

To compare the results of the tangent modulus G_t, Equation (2.22), with the secant modulus (2.27), we obtain the nondimensionalized secant modulus by appropriate manipulation of Equation (2.20) as

$$\frac{G_s}{G_0} = \frac{\tau_{octp}}{G_0} \frac{1}{\gamma_{oct}} \left[1 - exp\left(-\frac{G_0}{\tau_{octp}} \gamma_{oct}\right)\right] \tag{2.28}$$

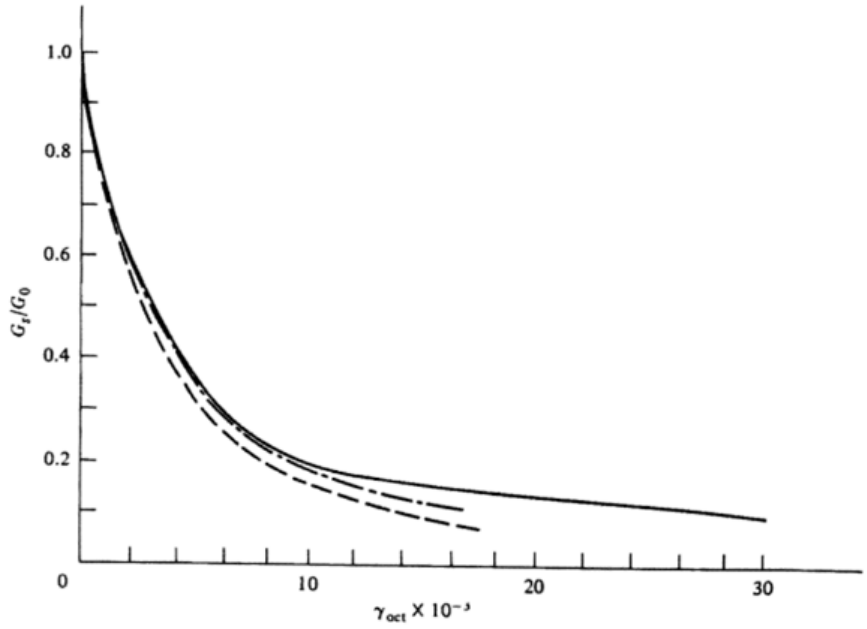

Figure 2.18 Variation of secant shear modulus: solid curve, Cedolin et al. (1977); dashed curve, Gerstle (1981, eq. 2.28, τ_{oct_p} = 2.32 kips/in²); dot-dash curve, Gerstle (1981, eq. 2.28, τ_{oct_p} = 2.55 kips/in²).

For the concrete used in the tests by Gerstle et al. (1978) and Grestle (1981) $2G_0$=2.9×10^3 kips/in^2 (20×10^3 N/mm^2), and the deviator strength τ_{octp} varied between 2.32 and 2.55 kips/in^2 (16.0 to 37.1 N/mm^2), depending on the stress ratio. Inserting theses values in Equation (2.28) and plotting results in Figure (2.18) by the dash and dash-dot curves, we observe a close correlation between Cedolin's secant formulation over the major portion of the range of Gerstle's tangent formulation.

2.4 Triaxial Behaviour of Concrete

2.4.1 Triaxial tests

Stress-strain behaviour. Figures (2.19) shows typical stress-strain curves from the tests by Richart et al. (1928). Their tests were conducted at low or moderate volumetric compression (or confining) stresses. Balmer (1949) conducted triaxial tests at very high confining-stress levels (Figure 2.20). As these curves show, depending on the confining stress, concrete can act as a *quasi-brittle*, *plastic-softening*, or *plastic-hardening* material. This is because under higher confining stresses the possibility of bond cracking is greatly reduced and the failure mode shift from cleavage to crushing of cement paste. Figures (2.19) and (2.20) show that the axial strength increases with increasing confining pressure. Under very high confining stresses, extremely high strengths have been recorded (Figure 2.20).

Contrary to popular belief, concrete exhibits nonlinear stress-strain behaviour under hydrostatic compressive loading (Figure 2.21). The hydrostatic-pressure-volumetric-strain curve in Figure (2.21) shows a reversal in curvature on loading. On unloading, the slope is almost constant and is very close to the slope during initial loading, except for a sharp tail in the low-stress range similar to that of cyclic uniaxial case (Figure 2.2). Analysis of test data indicates that when it is subjected to a constant hydrostatic stress (or constant σ_{oct}) and an increasing shear or deviatoric stress (or τ_{oct}), concrete undergoes not only octahedral shear strain γ_{oct} but also consolidation in the form of compressive octahedral normal strain ϵ_{oct}.

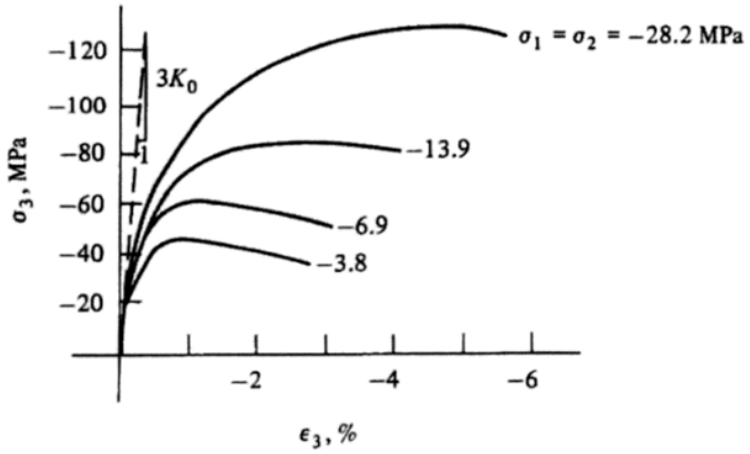

Figure 2.19 Triaxial compression test of concrete (K_0 = bulk modulus). *(Richart et al., 1928.)*

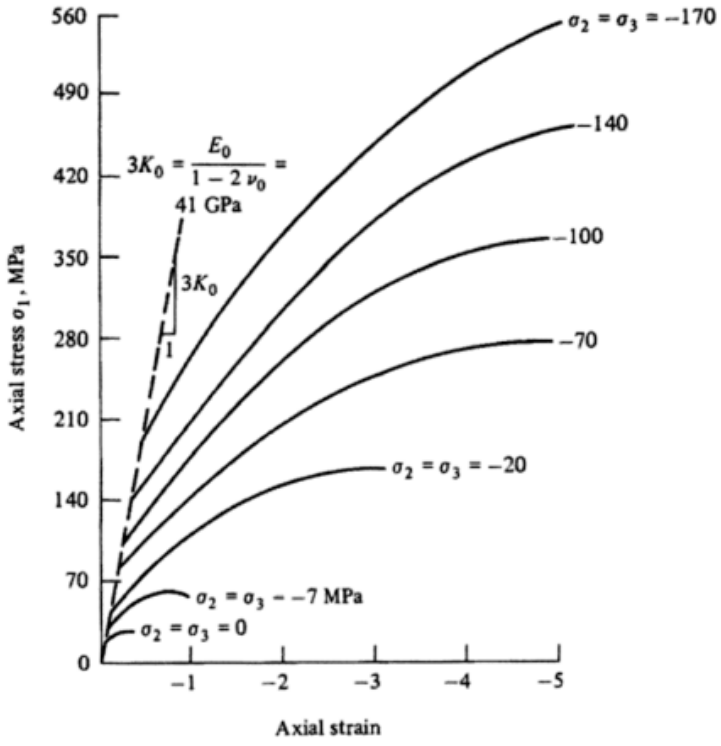

Figure 2.20 Triaxial stress-strain relationship for concrete. *(Balmer, 1949.)*

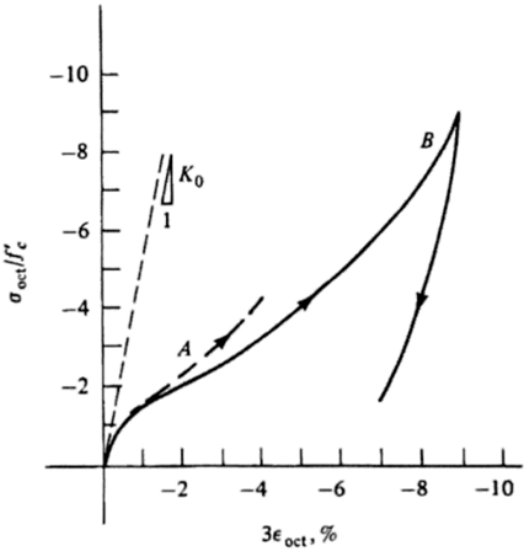

Figure 2.21 Behavior of concrete in hydrostatic compression ($\sigma_1 = \sigma_2 = \sigma_3$): *A* = Palaniswamy (1973), f'_c = 22 MPa; *B* = Green and Swanson (1973), f'_c = 48.5 MPa.

Failure surface. Under triaxial loading, experiments indicate that concrete has a fairly consistent failure surface that is a function of the three principal stresses. If isotropy is assumed, the *elastic limit* (onset of stable crack propagation), the onset of unstable crack propagation, and the *failure limit* all can be represented as surfaces in three-dimensional principal-stress space. Figure (2.22) shows schematically the elastic-limit surface and failure surface. For increasing hydrostatic compression (along the $\sigma_1 = \sigma_2 = \sigma_3$ axis), the deviatoric sections (planes perpendicular to the axis $\sigma_1 = \sigma_2 = \sigma_3$) of the failure surface are more or less circular, which indicates that the failure in this region is independent of the third stress

invariant. For smaller hydrostatic pressures, these deviatoric cross sections are convex and noncircular. The failure surface can be represented by three stress invariants.

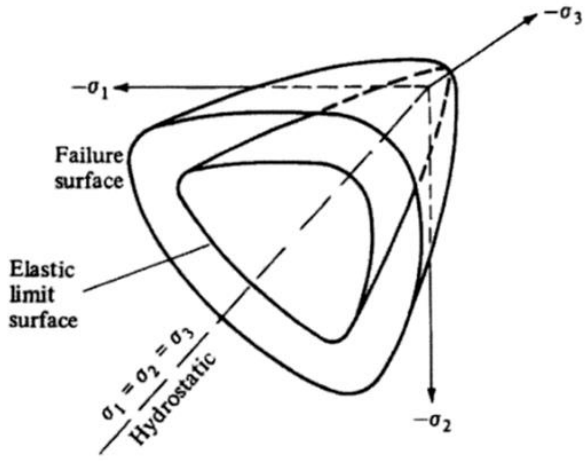

Figure 2.22 Schematic failure surface of concrete in three-dimensional stress space.

2.5 Stress-Strain Relations for Steel

2.5.1 General characteristics of reinforcing steel

Some typical stress-strain curves for different qualities of reinforcement steel are shown in Figure (2.24).

The stress-strain curves for steel are generally assumed to be identical in tension and compression. Also, if a steel specimen is loaded at a fast rate, the observed yield strength is a little higher. An increase of about 14% has been observed for a strain rate of 0.01 per second.

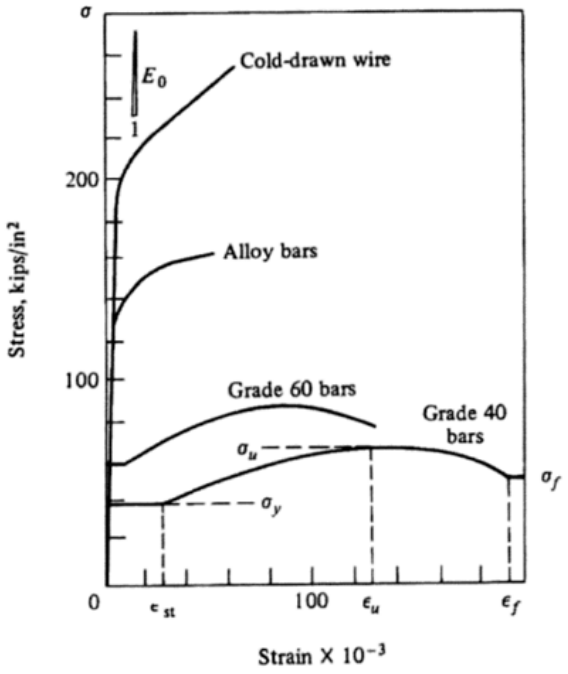

Figure 2.24 Typical stress-strain curves for steel reinforcement.

2.5.2 Reversed and repeated stress-strain behaviour

Stress-strain relationship for reinforcing steel in cyclic loading is considerably affected by previous plastic straining, as observed in Figure (2.25). A hot-rolled steel is loaded into the plastic region, whereupon cycles of unloading and reloading are performed. The pronounced feature of the cyclic stress-strain curves is the absence of the typical yield plateau observed in monotonic loading (Figure 2.24). The unloading portion of the curve is linear, and the slope is equal to the initial modulus of elasticity. Subsequent cycles have features similar to the first two cycles after the first load reversal. Note the unequal raising of the new yield points in loading and in reversed loading which define the subsequent linear-elastic portion of the stress-strain curve; i.e., a raising of the yield point in loading is followed by a lowering of the yield point when the stress is reversed. This is known as the *Bauschinger* effect. Figure (2.25) shows that the linear portion of the stress-strain curve is nearly constant during the cycles.

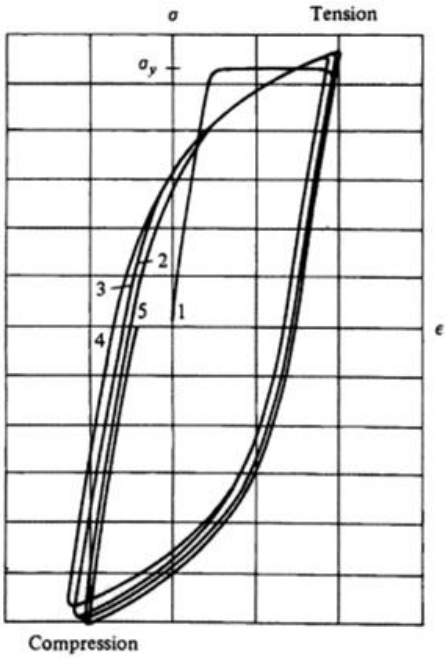

Figure 2.25 Stress-strain curve under cyclic loading. *(Singh et al., 1965.)*

2.5.3 Stress-strain models for reinforcing steel

Since steel-reinforcement elements in concrete construction are mostly one-dimensional, it is generally not necessary to introduce the complexities of multiaxial constitutive relationships for steel.

For simplicity in the design calculations, it is often necessary to idealize the one-dimensional stress-strain curve for steel. Three different idealizations, shown in Figure (2.26) have been used, depending on the accuracy required.

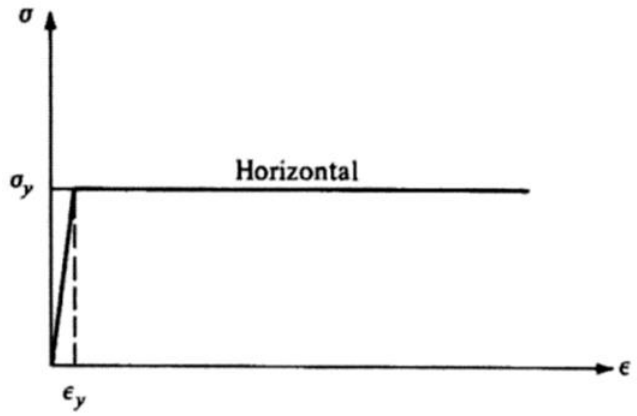

(a)

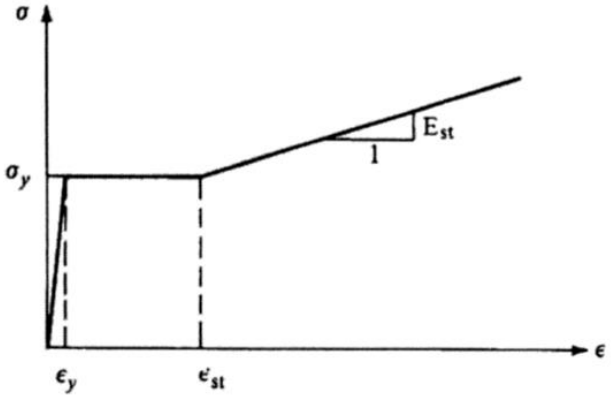

(b)

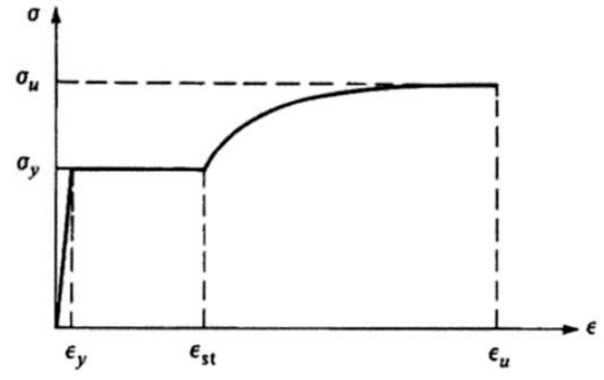

(c)

Figure 2.26 Idealizations for the stress-strain curve for steel in tension or compression: (*a*) elastic perfectly plastic approximation, (*b*) trilinear approximation, (*c*) complete curve.